

Unravelling the dynamic transition between supercapacitive and memristive states in solid-state nanostructured ZnO-based neuromorphic device by impedance spectroscopy

Cite as: J. Appl. Phys. **138**, 064502 (2025); doi: [10.1063/5.0282823](https://doi.org/10.1063/5.0282823)

Submitted: 28 May 2025 · Accepted: 22 July 2025 ·

Published Online: 8 August 2025



Simantini Majumdar^{1,2,a)}

AFFILIATIONS

¹Department of Energy, Politecnico di Milano, via Lambruschini 4, Milano 20156, Italy

²Chemistry and Physics of Materials Unit, Jawaharlal Nehru Centre for Advanced Scientific Research (JNCASR), Bengaluru 560064, India

^{a)}Author to whom correspondence should be addressed: simantini.energy@gmail.com

ABSTRACT

The integration of energy storage and memory functionalities within a single platform is a critical step toward developing compact, multi-functional, and energy-efficient electronic systems. Conventional architectures implement supercapacitive and memristive functionalities using separate components, which compromises system efficiency, increases design complexity, and limits real-time adaptability in applications such as neuromorphic computing and renewable energy systems. In this work, we present a dual-functional coin-type symmetric device that unifies energy storage and neuromorphic memory capabilities using a nanostructured porous ZnO electrode and a chitosan/polyvinylidene fluoride (CS/PVDF) solid polymer blend electrolyte. The device demonstrates stable supercapacitive performance within a 4 V electrochemical window and exhibits clear memristive behavior at higher voltages under specific current compliances. The device transitions seamlessly between high and low resistance states under controlled pulse sequences, emulating various brain-inspired synaptic activities, such as short-term and long-term potentiation (STP and LTP) behaviors. Impedance spectroscopy, analyzed through the Havriliak–Negami model, reveals non-Debye relaxation dynamics and voltage-dependent ion-electron transport, offering valuable insights into the frequency-domain behavior underpinning the state transitions. This spectroscopic approach provides a deeper understanding of the dynamic switching mechanisms, highlighting the interplay between ionic mobility and electronic conduction across the device states. The unique neuromorphic characteristics combined with energy storage functionality in a single architecture mark a significant advancement in the physics and engineering of next-generation devices. This work lays the foundation for developing bio-inspired, low-power electronics that are both functionally versatile and physically compact, with promising implications for artificial intelligence hardware and integrated energy systems.

© 2025 Author(s). All article content, except where otherwise noted, is licensed under a Creative Commons Attribution-NonCommercial-NoDerivs 4.0 International (CC BY-NC-ND) license (<https://creativecommons.org/licenses/by-nc-nd/4.0/>). <https://doi.org/10.1063/5.0282823>

I. INTRODUCTION

The exponential growth of data in modern society has intensified the demand for technologies capable of efficiently processing and storing vast volumes of information. Concurrently, the surging need for high-performance, compact, and multifunctional electronic devices has accelerated research into advanced energy storage and neuromorphic computing systems. Conventional computer architectures, based on the von Neumann model, encounter significant bottlenecks due to the inherent separation between storage

and computational units, which limits data transfer efficiency—an increasingly critical shortcoming in the Big Data era.^{1,2} The human brain, with its intricate network of billions of neurons interconnected by trillions of synapses, exemplifies efficient information processing, achieving complex cognitive functions like language, memory, and behavior with remarkable efficacy. Consequently, developing brain-inspired computing systems is vital for bridging the gap between current technologies and these growing demands. Neuromorphic computing, particularly with memristor-based architectures, presents a

16 August 2025 05:16:43

compelling avenue for emulating brain-like efficiency. These emerging hardware systems demonstrate capabilities in tasks such as data classification, pattern recognition, and unsupervised learning, underscoring the potential of memristors to tackle sophisticated cognitive functions.^{3–5} By mimicking biological synaptic functionalities such as short-term plasticity, long-term potentiation, and spike-time-dependent plasticity, these devices are poised to form the backbone of artificial intelligence and future autonomous systems. By advancing such neuromorphic prototypes, we can pave the way toward next-generation computational systems that harness the distinctive attributes of memristors for efficient, brain-inspired performance while enhancing computational density and reducing power consumption. Memristors exhibit unique properties that allow for both data storage and processing within a single device by adjusting resistance through various conductance states.^{6,7} As artificial synapses, memristors represent a compelling avenue for emulating synaptic weight changes found in biological neural networks. Research has explored a range of materials such as transition metal oxides, perovskites, and organic compounds to develop memristive devices suited for neuromorphic applications.^{8–10} Among these materials, binary oxides have shown strong performance in terms of endurance, fast switching, and memory retention. However, the variations in filament formation and rupture can lead to non-uniform resistive switching (RS) properties, complicating the deployment of memristors in non-volatile memory and neuromorphic circuits.¹¹ For effective neuromorphic integration, memristive devices require gradual and predictable switching behavior.

Complementing the capabilities of neuromorphic devices, supercapacitors present robust solutions for high-power energy storage with rapid charge–discharge cycles and exceptional longevity. The efficiency of these devices is closely linked to the electron flow and conductivity of the electrode materials used within them, making electrode optimization a priority for enhancing device performance.^{12–18} A promising and efficient approach to electrode design is the functionalization of nanomaterials, as nano-scaled materials possess increased active surface areas that can significantly enhance the electronic conductivity and capacitance of the electrode.^{19,20} Extensive research has been conducted on a range of highly electroactive nanomaterials to improve the performance of the supercapacitors over the years. Electrochemical double-layer capacitors (EDLCs), a prominent class of supercapacitors, which incorporate the use of carbon-based nanomaterials owing to their high pore volume and large surface area, store energy through physisorption at the interface of the electrode and electrolyte, facilitating rapid ion exchange and offering higher power densities suited for applications requiring swift energy bursts, such as hybrid electric vehicles, portable electronics, and grid storage solutions.^{21–23} Another class of nanomaterials, transition metal oxides (TMOs), has shown exceptional promise for use in pseudocapacitors (PCs), due to their excellent specific capacitance and energy density properties.¹⁶ Unlike EDLCs, which rely on physical ion adsorption, PCs store charge via Faradaic redox reactions at the electrode surface. These rapid redox reactions enable PCs with higher energy densities and specific capacitance than EDLCs, making them a superior option for applications requiring fast and efficient energy storage. The effectiveness of PCs, however, heavily depends on the intrinsic properties and structure of the electrode material.^{19,20} TMOs with variable

oxidation states have emerged as leading candidates for PC electrodes, as they provide multiple oxidation states that facilitate efficient redox ion exchange. Within the TMO category, zinc oxide (ZnO) has gained particular attention as an electrode material for PCs due to its high electrochemical activity, specific capacitance, and cost-effectiveness.^{24–28} Furthermore, solid polymer electrolytes (SPEs) can enhance supercapacitor performance by providing a leakage-free, thermally stable, and biodegradable alternative to traditional liquid electrolytes.^{29–33} However, SPEs, such as those incorporating either chitosan (CS) or polyvinylidene fluoride (PVDF), face limitations in room-temperature ionic conductivity, necessitating the integration of plasticizers, dopants, and polymer blends to enhance conductivity and mechanical robustness.¹⁵

While supercapacitor and neuromorphic technologies have each experienced substantial advancements, only a very few studies have integrated both the functionalities within a single device.^{34,35} This lack of combined functionality limits the potential for multifunctional systems capable of simultaneously achieving efficient data processing and robust energy storage. The key challenges include maintaining stable performance across extended cycles, achieving scalable architectures, and ensuring precise control over switching properties. Addressing these limitations is essential for realizing unified systems that meet the growing demands of high-performance, low-power electronic applications. Consequently, advancements in combining neuromorphic computing with high-capacity energy storage technologies promise to revolutionize the future of electronic devices and systems. These aspects have set the scope of the present work.

In the present work, we introduce a novel coin-type device combining supercapacitive and memristive functions, fabricated using a simple cost-effective method leveraging ZnO nanostructures and a blended CS/PVDF SPE matrix. Electrochemical impedance spectroscopy (EIS) is employed to reveal critical insights into the device's ionic and electronic transport, with low resistance values and stable ion diffusion characteristics affirming its suitability for both capacitive and memristive applications. Through comprehensive electrochemical testing, including impedance analysis, we demonstrate that this device exhibits high areal capacitance, a wide stability window, and synaptic-like behaviors under pulsed electrical stimuli. The results underscore the potential of the device as a multifunctional platform for both energy storage and neuromorphic computing, paving the way for advanced, integrated electronic systems.

II. RESULTS AND DISCUSSION

The steps involved in the fabrication of the coin-type symmetric dual-functional device are shown schematically in Fig. 1(a). Briefly, the cathode/anode was prepared by depositing a ~5 nm thin Ti and ~30 nm thin Au films (acting as a current collector) on the glass substrate, followed by spin coating of the Zn precursor (see Sec. IV for the synthesis details). The latter, upon annealing at 400 °C for 5 min, produced a porous ZnO nanostructure [as evident from the FESEM images in Fig. 1(c)], which can provide a large active surface area for electrochemical energy storage applications.

The ZnO film was characterized using XRD. The diffraction peaks of ZnO as illustrated in the inset of Fig. 1(c) exhibit a

16 August 2025 05:16:43

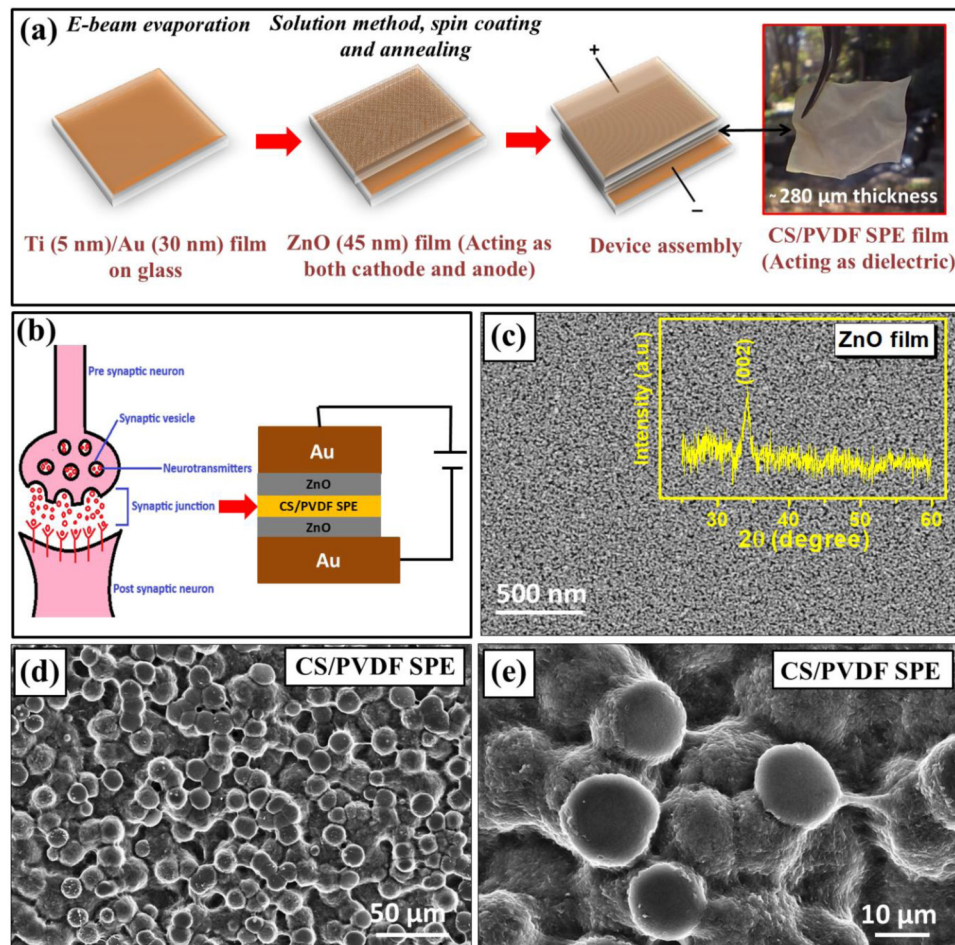


FIG. 1. (a) Schematic of the stepwise fabrication of the coin-type symmetric dual-functional device, with the photograph of the CS/PVDF solid polymer electrolyte (SPE) film (right), (b) schematic depicting the correlation between the coin-type synaptic device and the biological synapse, (c) FESEM images depicting the porous nanostructure of the ZnO film; inset: XRD of the ZnO film, and (d) and (e) FESEM images depicting the spherulite structure of the CS/PVDF SPE film.

single-phase wurtzite structure (space group $p6_3mc$, JCPDS #36-1451). The broad and low-intensity diffraction peak centered at $2\theta \approx 34.5^\circ$, corresponding to the (002) plane of the hexagonal wurtzite phase, suggests a preferential c-axis orientation of the ZnO crystallites. The estimated crystallite size calculated using the Scherrer equation is ~ 10 nm, suggesting the presence of microstrain and lattice disorder due to the relatively low annealing temperature and short processing duration. The broadness of this peak indicates a nanocrystalline or partially amorphous structure, which is likely due to the relatively low annealing temperature (400 °C) and short annealing time (5 min) employed during film processing. Such thermal conditions are insufficient for complete grain growth and crystallization, often resulting in lattice disorder and reduced crystallite size. Despite the limited crystallinity, this structural configuration is favorable for electrochemical applications, as the associated high defect density and increased surface area enhance ionic diffusion and promote surface-driven redox activity, both of which are critical for high-performance energy storage systems. The device fabrication was completed by sandwiching a ~ 280 μm thick blended chitosan (CS)/polyvinylidene fluoride (PVDF) solid

polymer blend electrolyte (SPE) film (see Sec. IV for the synthesis details) between the two electrodes [photograph of the free-standing SPE is shown in the inset of Fig. 1(a)].

The response of the coin-type symmetric device to electrical stimuli can be viewed as analogous to a biological synapse, as illustrated in Fig. 1(b). In this analogy, the cathode and anode resemble the biological neural network, while the solid polymer electrolyte resembles neural fluid, facilitating ion transport. The surface morphology of the blended CS/PVDF SPE was characterized by FESEM, which revealed the spherulitic microstructure characteristic of PVDF [Figs. 1(d) and 1(e)].³⁶ These well-defined, smooth spherulites observed are indicative of phase separation between CS and PVDF, where PVDF forms semi-crystalline spherulitic domains, while the surrounding rougher regions are attributed to the amorphous nature of CS. The interconnected nature of these spherulites, coupled with the porous regions that separate them, facilitates enhanced ionic mobility within the material.

The Differential Scanning Calorimetry (DSC) thermogram of the blended CS/PVDF SPE material is shown in Fig. 2(a). The thermogram reveals a prominent endothermic peak corresponding to

16 August 2025 05:16:43

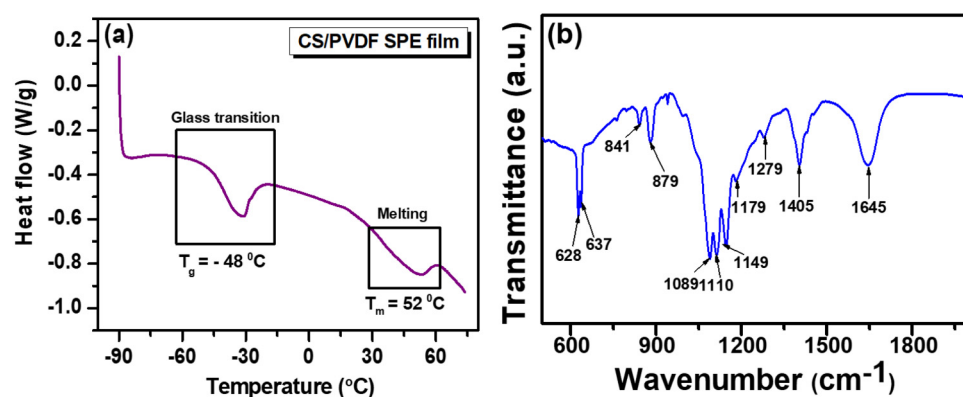


FIG. 2. (a) DSC thermogram of the CS/PVDF SPE film and (b) FTIR transmission spectrum of CS/PVDF SPE.

the melting temperature (T_m) of the crystalline phase of the polymers, determined to be 52 °C. Additionally, a distinct glass transition temperature (T_g) is observed at -48 °C, highlighting the increased amorphous nature of the system, which facilitates enhanced segmental motion of the polymer chains, contributing to improved ionic transport and high ionic conductivity of the material. FTIR spectroscopy is performed to study the complexation and interactions between the blended polymers, LiClO_4 , and glycerol, which can induce changes in the vibrational modes of the polymer molecules in the blended CS/PVDF SPE material. The FTIR transmission spectrum over the range of 500–2000 cm^{-1} for the blended CS/PVDF SPE is shown in Fig. 2(b). In the blended SPE system, the peaks near 628 and 637 cm^{-1} correspond to free and contact ion pairs, respectively.^{37,38} The bands around 879 and 1089 cm^{-1} are assigned to the α -phase of PVDF, while the bands around 841, 1179, 1279, and 1405 cm^{-1} are assigned to the β -phase of PVDF.^{39–46} The bands around 1149 and 1645 cm^{-1} are assigned to the stretching vibrations of C–O–C and secondary amide (R-CONH₂) of CS.⁴⁷ The band around 1110 cm^{-1} is assigned to the C–O stretching vibration modes of primary and secondary alcohols of glycerol.⁴⁸

The voltage window of a supercapacitor is defined as the range between the minimum and maximum voltages within which the device operates stably, without electrolyte decomposition or significant capacitance loss. To investigate the electrochemical performance of the as-fabricated device, we performed cyclic voltammetry (CV) of the device. We performed the CV scans by gradually increasing the voltage window from 1.4 to 8 V at scan rates varying from 50 to 500 mV/s [as shown in Figs. 3(a)–3(d) and Fig. S1 in the supplementary material]. In the voltage window of 1.4 V, a semi-rectangular shaped cyclic voltammogram is observed even at slower scan rates, ensuring excellent capacitive characteristics of the device [Fig. 3(a)].¹⁵ The curves remain nearly semi-rectangular even at faster scan rates, suggesting efficient ion transport within the device.^{15,17} This behavior reflects the accessible pore structures of ZnO, which enable the electrolyte ions from the blended CS/PVDF SPE to diffuse rapidly and maintain electrostatic interactions, even under high scan rate conditions. Such robust rate performance can be attributed to the high surface-to-volume ratio and the interconnected nanoporous architecture of the ZnO layer,

which collectively enhance ion accessibility, shorten diffusion pathways, and support efficient charge transport across the electrode–electrolyte interface.

On gradually increasing the voltage window to 2 and 4 V, respectively, the curves continued to be leaf-shaped at both slower and faster scan rates,¹⁵ indicating continued electrochemical stability of the device [as shown in Figs. 3(b) and 3(c)]. For voltage windows beyond 6 V, the CV loops become distorted with a fast increment in current at higher voltage, as shown in Fig. 3(d) and S1 (supplementary material), respectively.⁴⁹ This distortion at extended voltage windows reflects a deviation from ideal capacitive behavior, potentially due to electrolyte decomposition, faradaic side reactions, or field-induced charge accumulation at the electrode–electrolyte interface. Hence, the electrochemical stability window (ESW) of the as-fabricated device is found to be 4 V, while a maximum areal capacitance value of 0.88 mF/cm^2 is obtained at a scan rate of 50 mV/s in the ESW. Thus, the device behaved as a supercapacitor as expected. However, the abrupt rise in current in the voltage range of -2 to -3 V [as shown in the inset of Fig. 3(d)] motivated us to examine the possibility of employing it for memristive and neuromorphic studies.⁴⁹ This voltage-specific current surge points toward a possible resistive switching mechanism, likely driven by field-induced migration of ionic species or modulation of oxygen vacancies in the ZnO matrix. This observed transition is consistent with our earlier findings,⁴⁹ where similar characteristics appeared in a different ionogel system under high-voltage stress, reinforcing the dual-functional potential of the present device. This way, the electrochemical potential window (6 V) can serve depending upon the current compliance, for both the supercapacitor and the memristor.

The applicability of the as-fabricated supercapacitor device is evaluated through the galvanostatic charge–discharge (GCD) technique. The device has been charged and discharged at a constant current density of 60 $\mu\text{A}/\text{cm}^2$ within a potential range of -1 to +1 V and -2 to +2 V, respectively. As shown in Fig. 4(a), GCD curves of the as-fabricated supercapacitor device exhibited a semi-triangular feature with different potential windows, which indicates good capacitive behavior. A maximum areal capacitance value of 1.66 mF/cm^2 is obtained in the ESW. This semi-triangular shape can be attributed to a combination of electric double-layer formation on the porous ZnO surface and faradaic contributions, likely

16 August 2025 05:16:43

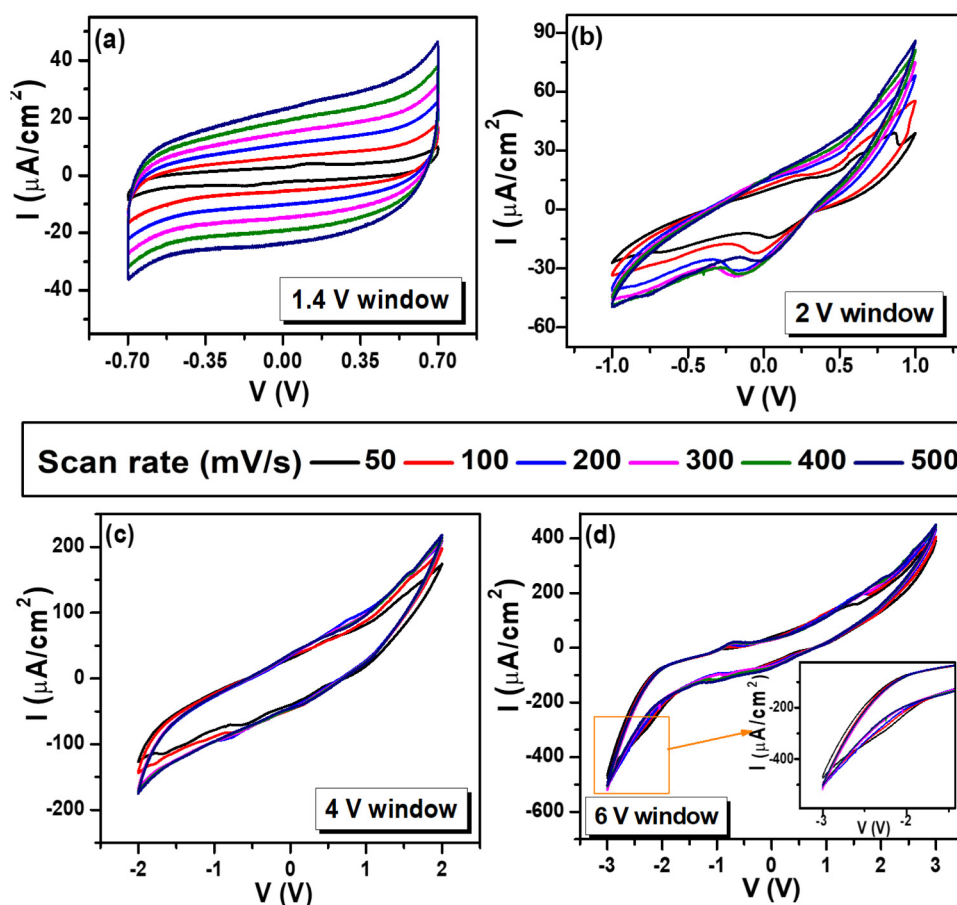


FIG. 3. (a)–(d) Scan rate-dependent cyclic voltammetry of the device measured at different voltage windows (1.4–6 V). Scan rates vary from 50 to 500 mV/s.

enabled by the nanostructured morphology that provides redox-active sites. The heterogeneous structure of the CS/PVDF SPE³⁶ supports this behavior by facilitating both ionic transport and interfacial charge interactions, leading to the observed quasi-ideal capacitive response.

Electrochemical impedance spectroscopy (EIS) has been performed to gain information regarding the kinetics of the solid electrolyte ions responsible for charge accumulation. The Nyquist plot of the as-fabricated device over a frequency range of 40 kHz to 1 Hz is shown in Fig. 4(b). The variation of the imaginary part of impedance (Z_{im}) exhibits a diagonally inclined line rather than a perfectly vertical one, indicating a combination of capacitive and diffusive behavior. This is consistent with the presence of Warburg impedance and non-ideal capacitive characteristics arising from the distributed nature of the porous electrode and the solid polymer electrolyte interface.

The impedance data [Fig. 4(b)] were analyzed using the Randles equivalent circuit comprised of R_s , R_{ct} , W , C_{dl} , and C_{FS} as shown in Fig. S2 (supplementary material). R_s represents the contact resistance between the current collector and electrode and that with the electrode and electrolyte. R_{ct} denotes the charge transfer resistance, and W is the Warburg impedance. C_{dl} and C_{FS}

represent the electric double-layer capacitance and the pseudocapacitance, which accounts for the faradaic reactions inside the electrode. The Warburg impedance (W) is related to the diffusion of ions in the electrode pores. The low values of R_s ($\sim 5.6 \Omega$) and R_{ct} ($\sim 3.4 \Omega$) indicate, respectively, the presence of an intimate contact between the electrode and the electrolyte and a facile ion diffusion at the interfacial region. The absence of a pronounced semicircle in the high-frequency region supports the low R_{ct} and further confirms efficient charge transfer kinetics. These values are consistent with the highly accessible porous ZnO surface and the amorphous-rich regions in the SPE that together contribute to efficient charge storage and transport. The nanoporous morphology of ZnO offers an extensive interfacial area, allowing more active sites for electric double-layer formation and facilitating fast electrolyte ion diffusion into the electrode. Simultaneously, the amorphous regions within the CS/PVDF solid polymer electrolyte serve as flexible pathways for ion migration, reducing the bulk ionic resistance. The combination of these morphological features ensures rapid ion exchange across the electrode–electrolyte interface, supporting both low charge transfer resistance and enhanced capacitive behavior.

The frequency dependence of the real (C_{re} ; the usable capacitance of the device) and imaginary (C_{im}) parts of the capacitance is

16 August 2025 05:16:43

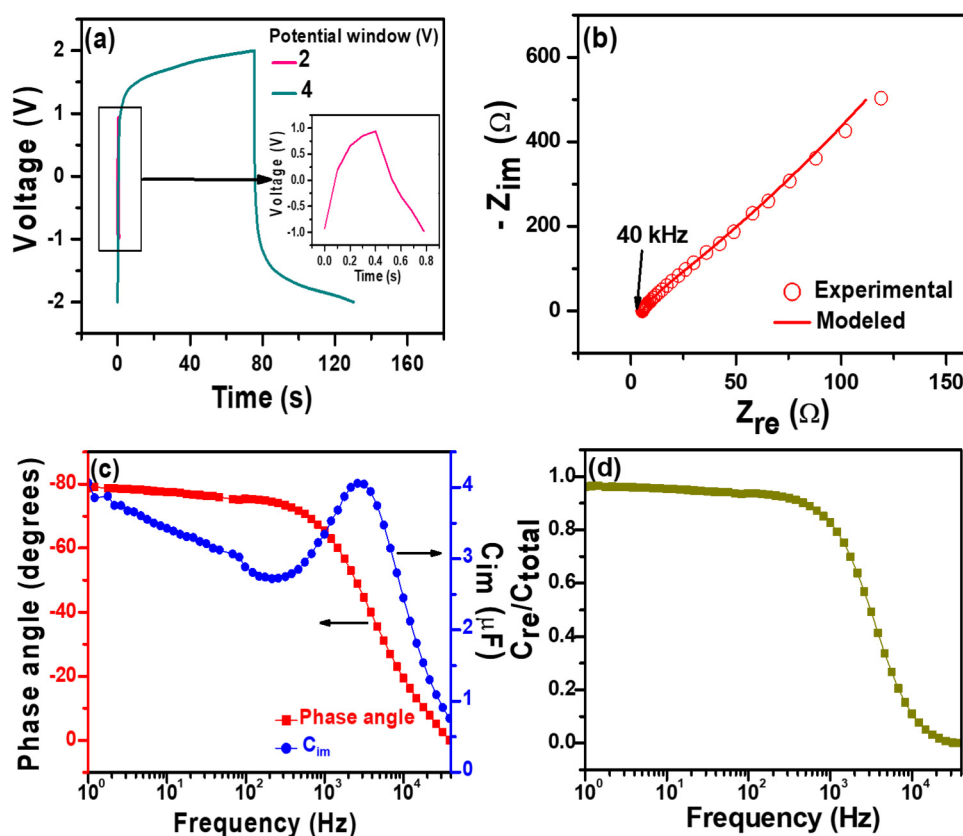


FIG. 4. (a) Galvanostatic charge-discharge curve of the device measured at a fixed current density of $60 \mu\text{A}/\text{cm}^2$ under varying potential windows (2 and 4 V). Impedance analysis of the device. (b) Nyquist plot of the device over a frequency range of 40 kHz to 1 Hz, (c) Bode phase plot and C_{im} variation with frequency, and (d) $C_{\text{re}}/C_{\text{total}}$ variation with frequency of the as-fabricated device.

shown in Fig. S3 (supplementary material) and Fig. 4(c), respectively. The values of C_{re} mainly depend on the electrode nanostructure and the electrode-electrolyte interface. As shown in Fig. S3 (supplementary material), C_{re} tends to increase at the low-frequency region ($\sim 0.02 \text{ mF}$ at 1 Hz) since electrolyte ions are having sufficient time to reach the nanoporous ZnO structure, while at higher frequencies, C_{re} tends to have a very low value ($\sim 0.56 \text{ nF}$), indicating a resistor-like nature. This frequency-dependent behavior reflects the morphological influence of both the ZnO and the SPE: the former enabling effective charge accumulation at low frequencies through its porous network, and the latter maintaining consistent ion conduction even as the frequency increases.

In the Bode plot [as shown in Fig. 4(c)], the phase angle for the device is quite high at lower side frequencies and the largest phase angle $\sim -80^\circ$ is observed, inferring excellent capacitive performance of this device. The phase angle tends to be zero at higher frequencies since the device changed their nature from capacitive to pseudo-inductive and hence at higher frequencies above 40 kHz, Z_{im} attains a positive value. The frequency where Z_{im} changes its sign is known as the resonance frequency (f_r), which is found to be $\sim 42 \text{ kHz}$ for the device under study. The variation of C_{im} with frequency [as shown in Fig. 4(c)] shows a relaxation peak at $\sim 2.879 \text{ KHz}$. This is the frequency below which the device is dominantly capacitive in nature, while above which the resistive nature

is dominated.²⁹ The reciprocal of this relaxation frequency gives the time constant (τ_0) of the device, which is found to be 0.35 ms. The total capacitance (C_{total}) of the device can be estimated from Z_{im} using the following equation, $C_{\text{total}}(\omega) = -1/\omega Z_{\text{im}}(\omega)$. The variation of $C_{\text{re}}/C_{\text{total}}$ with frequency for the device is shown in Fig. 4(d). The $C_{\text{re}}/C_{\text{total}}$ ratio is ~ 0.962 , which is closer to 1, confirming the good polarizability of the device and almost all the capacitance is usable. This high capacitive utilization ratio is a direct consequence of the well-integrated porous ZnO electrode structure and phase-separated ionic pathways within the CS/PVDF blended solid polymer electrolyte,³⁶ which together minimize losses and ensure efficient charge accumulation and transport throughout the device.

I-V sweep measurements were performed on the device in the sweep range of -3 to $+3 \text{ V}$ (i.e., a voltage window of 6 V) at varying current compliances (I_{cc}). It is an interesting feature of the device that it exhibits a capacitive behavior until $I_{\text{cc}} = 50 \mu\text{A}$, while the device switches to memristive characteristic behavior at $I_{\text{cc}} \geq 100 \mu\text{A}$, as shown in Figs. 5(a) and 5(b), respectively.⁵⁰ At $I_{\text{cc}} = 50 \mu\text{A}$, the lack of a hysteresis loop confirms that no permanent conductive path is formed, and the current remains governed by pure ionic transport within the electrolyte. Although the device started switching from high resistance state (HRS) to low resistance state (LRS) at $100 \mu\text{A}$, the typical pinched hysteresis loop (with zero crossing) as expected for a memristor is observed at $I_{\text{cc}} \geq 200 \mu\text{A}$ [shown in Fig. 5(b)].⁵⁰ As I_{cc} reaches $100 \mu\text{A}$, partial filament

16 August 2025 05:16:43

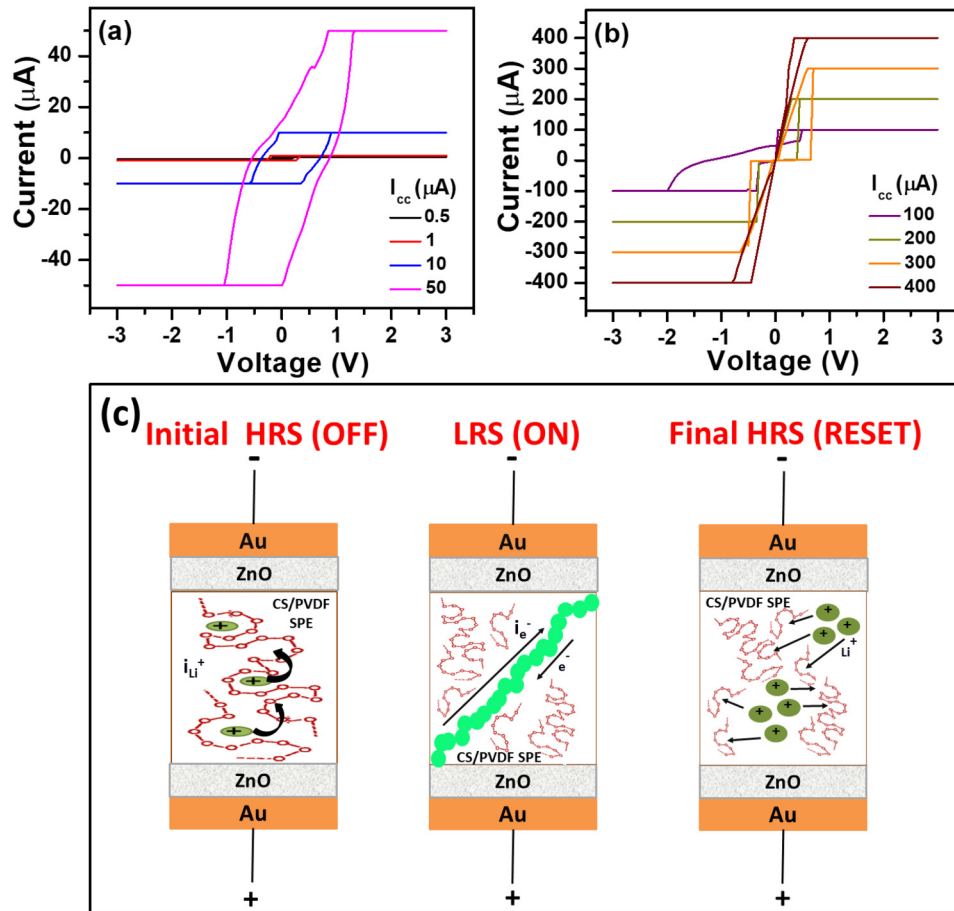


FIG. 5. I-V sweeps of the device at different current compliance (I_{cc}) values. (a) 0.5–50 μA , (b) 100–400 μA , (c) schematic illustrating the internal physical processes in the as-fabricated device under applied electric bias: in the initial HRS (OFF state), Li^+ ions in CS/PVDF SPE migrate through the matrix via hopping, resulting in ionic conduction; upon reaching a threshold bias, Li^+ ions reduce at the ZnO cathode forming metallic lithium filaments that establish an electronic conductive path, switching the device to the LRS (ON state) during the SET process; when the bias is removed or reversed, filament dissolution occurs restoring the device to the HRS in the RESET process.

formation results in a nonlinear I-V response with memory characteristics, yet without a zero crossing, indicating the onset of resistive switching behavior, though not yet fully memristive. The I-V curve at $I_{cc} = 100 \mu\text{A}$ demonstrates a non-zero cross-point voltage [as shown in Fig. 5(b)], which satisfies the history-dependent memristor nature.⁵⁰ However, a fully developed pinched hysteresis loop, commonly regarded as the definitive fingerprint of memristive systems is clearly visible at $I_{cc} \geq 200 \mu\text{A}$, confirming a transition to stable and reversible switching. In the HRS, under the application of an electric field, the Li^+ ions in the SPE are transported along the free volumes provided through the random motion of the polymer chains. At this state, the current in the as-fabricated device is controlled by the ionic conduction of the Li^+ ions [Fig. 5(c)]. The Li^+ ions are migrated toward the ZnO cathode where they are reduced to metallic Li. At the threshold voltage (V_{th}), the lithium filament starts to grow and penetrates the SPE to form an electronic conductive path, which switches the device to the LRS [Fig. 5(c)]. This stepwise evolution in switching characteristics with increasing current compliance is a strong indicator of memristive behavior, where filamentary conduction is modulated by field-driven Li^+ ion migration. The variation of V_{th} with current compliance is shown in Fig. S4 (supplementary material). The threshold voltage (V_{th}) of

the device is found to be very low (i.e., $V_{th} < 1 \text{ V}$) at different current compliances.

We further investigated the dependence of current on voltage scan rates. At I_{cc} of $100 \mu\text{A}$, the I-V curves obtained in the sweep range of -3 to $+3 \text{ V}$ show a non-zero crossing or non-pinched current-voltage hysteresis behavior [as shown in Fig. 6(a)]. This can be attributed to the involvement of the capacitive effect (owing to the presence of the ZnO layer) and the appearance of ferroelectric polarization (owing to the presence of ferroelectric PVDF polymer in the SPE layer) at lower current compliance. Although at higher compliances of $I_{cc} \geq 200 \mu\text{A}$, a zero-crossing pinched current-voltage hysteresis loop is observed, as shown in Figs. 6(b)–6(d), respectively.

The areas inside the I-V hysteresis loops (S) at $I_{cc} = 200 \mu\text{A}$ are comparable to each other at faster voltage scan rates [as shown in Fig. S5(b) in the supplementary material]. But at slower voltage scan rates, a noticeable fluctuation in the value of S is observed, irrespective of the current compliance values [Figs. S5(a)–S5(d) in the supplementary material]. However, at higher I_{cc} ($\geq 250 \mu\text{A}$), the I-V curve exhibits a transition in the shape with respect to the scan rate, from a hysteresis loop at slower scan rates to a linear form at faster rates [Figs. 6(c) and 6(d)]. The area inside the hysteresis

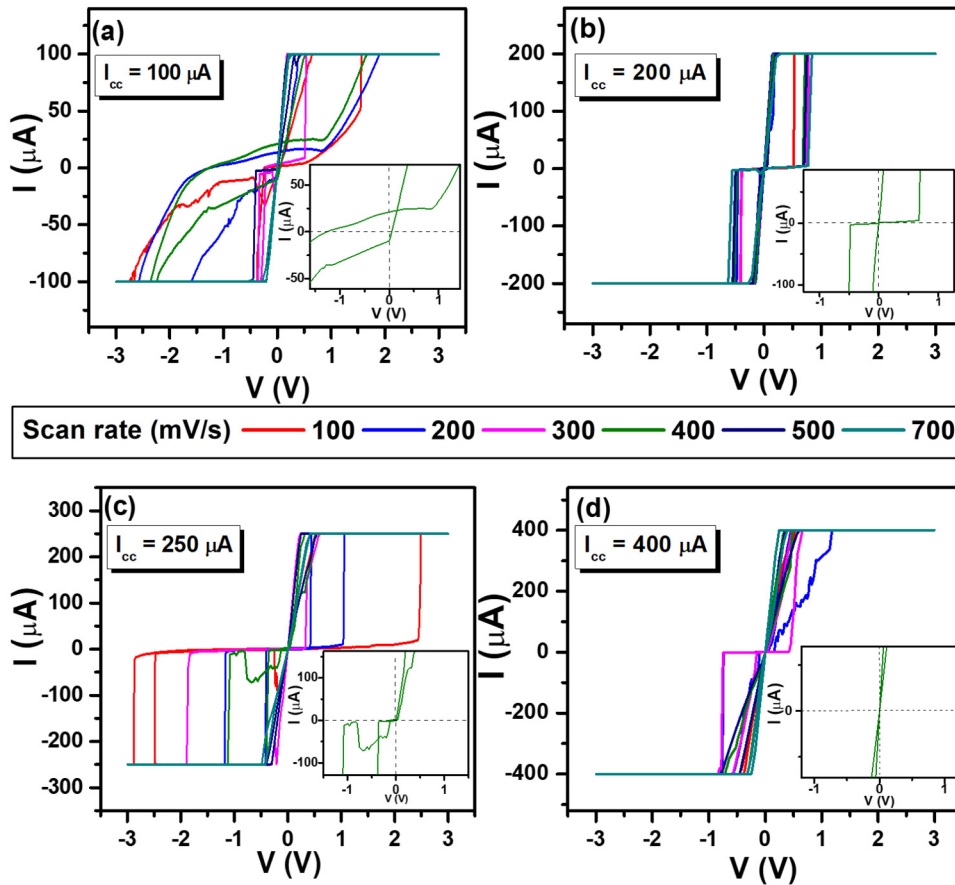
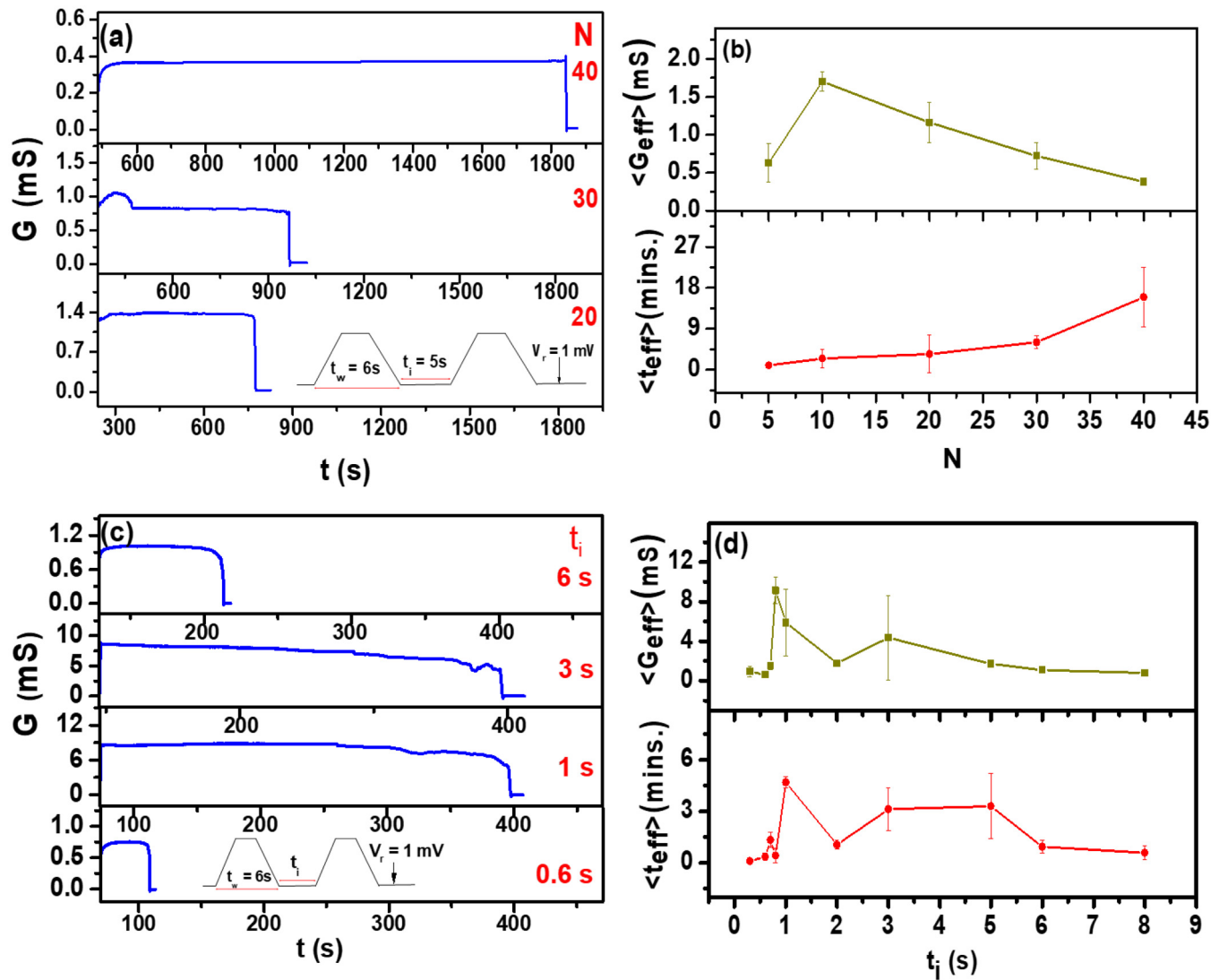


FIG. 6. (a)–(d) I–V sweep of the device at I_{cc} of 100, 200, 250, and 400 μA , performed at varying scan rates (100–700 mV/s). The inset shows the enlarged view of the I–V at a scan rate of 400 mV/s around the origin.

loop (S) shrinks as the voltage scan rate increases from 300 mV/s and degenerates almost to zero at a faster scan rate of 700 mV/s, as shown in Figs. S5(c) and S5(d) in the [supplementary material](#). The pinched hysteresis loop, reduced loop area with increasing scan rate, and the linear I–V relationship at faster scan rates satisfy the three fingerprints of a good memristive device. However, the transition from the hysteresis loop to the linear characteristic behavior is not observed in the studied voltage scanning rates at $I_{cc} = 200 \mu A$. This gives us a larger voltage scanning frequency range to study the neuromorphic behavior of this memristive device.

The memory behavior in the as-fabricated device, analogous to a biological synapse [Fig. 1(b)], is further investigated by applying the electrical pulses. The pulse sequence was designed after careful examination of the I–V sweep of the device at different voltage scanning rates, which employs electrical pulses of 2 V amplitude with 6 s width and 5 s as an interval. The chosen pulse sequence was applied with a background reading voltage of 1 mV as shown in the bottom panel of Fig. 7(a), with a current compliance of 200 μA . On application of the defined pulse sequence, the device switches from HRS to LRS limited by the set I_{cc} and the conductance state is found to be retained beyond the pulse sequence at varying number of pulses (N), as shown in Fig. S6 ([supplementary material](#)) and Fig. 7(a), from 1 min (for $N = 5$

pulses) to 16 min (for $N = 40$ pulses), before decaying back to HRS, thus emulating long-term potentiation (LTP) behavior in the device. As shown in the bottom panel of Fig. 7(b), it is observed that the effective retention time (t_{eff}) increases gradually with increasing number of pulses (N), which has been calculated using the following equation, $t_{eff} = \frac{\sum_{i=0}^N G_i t_{ni}}{G_{max}}$, where G_{max} is the maximum value of the conductance during the period of retention in the absence of the pulse train. This indicates the formation of a conducting filamentary path in the device [Fig. 5(c)] that are less likely to get dissolved beyond the pulse sequence on increasing the number of pulses, resulting in a gradual enhancement of the effective retention time in the device. It is well known that the free Li^+ cations have greater mobility than free ClO_4^- anions. Hence, the polar amine and amide functional groups present in the SPE, which act as dipoles under an electric field, interact with the Li^+ cations due to the Coulombic force. This interaction of the amine and amide bands with the Li^+ cations aids in their transport by inter-chain and intra-chain ion hopping during polymer segmental motion in the HRS [Fig. 5(c)], resulting in higher ionic conductivity of the system (as evident from AC impedance spectroscopy studies, discussed later in this section). These Li^+ cations are reduced to metallic Li at the ZnO cathode. Next, when the device



16 August 2025 05:16:43

FIG. 7. Synaptic behavior emulated with pulsed voltage signals with varying number of pulses at a current compliance of $200\text{ }\mu\text{A}$. (a) Variations in conductance (G) with varying number of pulses, $N = 20, 30$, and 40 , respectively, after the applied pulse sequence ends. Long-term potentiation is emulated with varying number of pulses; inset shows the voltage signal of 2 V amplitude having pulse width (t_w) = 6 s , pulse interval (t_i) = 5 s , and a fixed reading voltage (V_r) of 1 mV . (b) variation of average effective retention time ($\langle t_{\text{eff}} \rangle$) and conductance ($\langle G_{\text{eff}} \rangle$) with pulse number (N), (c) variations in conductance (G) with pulsed voltage signals ($N = 10$) and varying pulse interval (t_i) at a current compliance of $200\text{ }\mu\text{A}$; the inset shows the voltage signal of 2 V amplitude, pulse width (t_w) = 6 s , and a fixed reading voltage (V_r) = 1 mV . Short-term potentiation (STP) and long-term potentiation (LTP) can be emulated with varying pulse interval (t_i), (d) variation of average effective retention time ($\langle t_{\text{eff}} \rangle$) and conductance ($\langle G_{\text{eff}} \rangle$) with pulse interval (t_i).

switches to LRS at a voltage amplitude of 2 V , the Li filament starts growing and penetrating the SPE, resulting in the formation of electronically conductive filamentary paths connecting the two electrodes [Fig. 5(c)]. This leads to an overall decrease in the ionic conductivity of the system in the LRS, while the voltage pulses are withdrawn, the Li filaments tend to break and relax back to the HRS [Fig. 5(c)], resulting in an increase in the ionic conductivity (as confirmed using AC impedance spectroscopy studies, discussed

later in this section). The relaxation behavior of the SPE ions in the as-fabricated device at both HRS and LRS has been discussed in detail later in this section using AC impedance spectroscopy. The conductive Li filament formation in the SPE connecting the cathode and the anode at LRS, as allowed by the set current compliance (I_{cc}), was examined in terms of the effective conductance (G_{eff}) of the device [as shown in the top panel of Fig. 7(b)]. The effective conductance value (G_{eff}) has been determined using the

following equation, $G_{\text{eff}} = \frac{\sum_{i=0}^n G_i t_{\text{mi}}}{t_{\text{total}}}$, where t_{total} is the total time until the device remains in the LRS in the absence of the pulse sequence. It is observed that the value of G_{eff} is maximum (~ 1.7 mS) at $N = 10$ [as shown in Fig. 7(b)], while it decreases gradually and becomes minimum ($\sim 380 \mu\text{S}$) at $N = 40$. This indicates that although the conducting filaments in the device does not dissolve with increasing number of pulses (N) even beyond the pulse train duration, the strength of the formed filaments is comparatively thin and weaker beyond $N = 10$. Thus, $N = 10$ is found to be the optimal number of pulses for carrying out further studies since the conducting filaments which are formed under this condition are thick and stable and can be maintained for a longer period emulating LTP behavior.

The memory behavior in the device is further examined by applying 10 consecutive 6 s electrical pulses of 2 V amplitude at a current compliance of $200 \mu\text{A}$ with varying interval (t_i) ranging from 0.3 to 8 s, while reading the conductance state at 1 mV [as shown in Fig. 7(c) and Fig. S7 in the supplementary material]. For a low pulse interval (t_i) of 0.6 s, the device shows conductance retention of ~ 21 s, thereby emulating STP behavior [bottom panel of Fig. 7(c)]. On increasing pulse interval (t_i) to 1 s, a transition to LTP behavior is observed with a conductance retention of ~ 5 min [Fig. 7(c)], which was almost maintained until $t_i = 5$ s. However, a transition from LTP to STP is observed at $t_i \geq 6$ s [top panel of Fig. 7(c)]. This indicates that the optimum range of t_i for the formation of a stable conducting filament in the device lies between $1 \leq t_i \leq 5$. This filament formation could be explained in terms of the effective conductance (G_{eff}) of the device. It is found that G_{eff} becomes maximum (~ 9.14 mS) at $t_i = 0.8$ s [as shown in Fig. 7(d)], while it decreases very gradually ($G_{\text{eff}} \sim 5.885$ mS at $t_i = 1$ s) and becomes minimum ($\sim 790 \mu\text{S}$) at $t_i = 8$ s. This suggests that the strength of the formed conducting Li filaments becomes thick and strong on increasing the pulse interval (t_i) up to a certain limit, above which they become again thin and weaker. Hence, it is of utmost importance to design the pulse sequence in an appropriate manner for the successful emulation of the stable LTP behavior in the as-fabricated device.

A schematic illustration is proposed to explain the switching mechanism and the underlying internal physical processes happening in the as-fabricated device with applied electric bias at initial HRS (OFF state), intermediate LRS (ON state), and final HRS (RESET state), as shown in Fig. 5(c). During HRS, under an applied electric bias, the lithium cations present in the SPE are transported by inter-chain and intra-chain ion hopping during polymer segmental motion toward the ZnO cathode, and hence the current in the device is dominated by Li^+ ionic conduction. This corresponds to the OFF state of the as-fabricated memristive device. At the ZnO cathode, the Li^+ ions are getting reduced to metallic Li and when the voltage bias is larger, i.e., at a voltage amplitude of 2 V, the device switches to LRS and at this state, the lithium filament starts to grow from the cathode and penetrates the SPE to form an electronic conductive filamentary path which connects both the electrodes. This stage corresponds to the SET process, i.e., the LRS or the ON state of the memristive device. Further on reducing the voltage bias, i.e., when the voltage pulses of the defined pulse sequence with a background reading voltage of

1 mV are withdrawn, the lithium filaments break and relax back again to the HRS. This corresponds to the RESET process, i.e., the OFF state of the device. If the applied number of pulses (N) and the pulse interval (t_i) in the defined pulse sequence is such that the lithium conducting filament becomes very strong and thick and the electrical potential is offset by the high electronic conductivity, the driving force cannot immediately strip lithium away from the filament on withdrawal of the voltage pulses, in order to break it for HRS, which results in an increase in the effective retention time, i.e., emulation of LTP behavior in the device.

To determine the extent of ionic and electronic contributions to the total conductance in the as-fabricated device during HRS (OFF state) and LRS (ON state), respectively, Wagner's DC polarization method has been used for determining the ionic transference number (t_{ion}). Ionic transference number is a very crucial parameter for ionic conductors, which gives the estimation of the fraction of conductivity due to the movement of the ionic species inside the SPE. A fixed dc voltage (10 mV) was applied to the device, and the current was measured as a function of time during HRS and LRS, respectively (as shown in Fig. S8 in the supplementary material). It is observed that the dc decreases gradually with time and becomes almost constant as polarization develops in the SPE during HRS. The ionic transference number can be calculated using the following equation, $t_{\text{ion}} = \frac{I_{\text{initial}} - I_{\text{final}}}{I_{\text{initial}}}$. The ionic transference number calculated at HRS comes as 0.76, which indicates predominant ionic conduction; while at LRS, the value is 0.005, inferring predominant electronic conduction in the device.

To probe the ionic conductivity and the ion relaxation dynamics in the as-fabricated memristive device at initial HRS (OFF state), intermediate LRS (ON state), and final HRS (RESET state), the frequency-dependent conductivity spectra have been examined. The AC conductivity has been calculated using the relation $\sigma(\omega) = \omega \epsilon_0 \epsilon_{\text{im}}$, where ϵ_0 is the vacuum permittivity (8.854×10^{-14} F/cm) and ϵ_{im} is the dielectric loss. The frequency-dependent AC conductivity spectra of the device at different states of the memristive device are shown in Fig. 8(a), at 300 K. A large dispersive region at lower frequencies followed by an almost frequency-independent plateau region has been observed during both initial and final HRS, while during LRS, the AC conductivity spectra show an almost frequency-independent plateau region in the low-frequency regime and a dispersive region at higher frequencies. The low-frequency dispersive region arises due to the charge-carrier accumulation at the electrode-SPE interface, while the plateau region almost independent of frequency corresponds to the ionic conduction in the device related to the hopping motion of the mobile Li^+ ions.

The AC conductivity of the device in the LRS can be explained based on Almond-West (AW) formalism, which is given by⁵¹

$$\sigma(\omega) = \sigma_{\text{ion}} \left[1 + \left(\frac{\omega}{\omega_p} \right)^n \right], \quad (1)$$

where n is the AW power law exponent, ω_p is the ion-hopping frequency, and σ_{ion} is the ionic conductivity of the Li^+ ions in the device. The best fit of the AC conductivity spectra at LRS based on Eq. (1) is shown in Fig. 8(a). A Li^+ ion can successfully hop from

16 August 2025 05:16:43

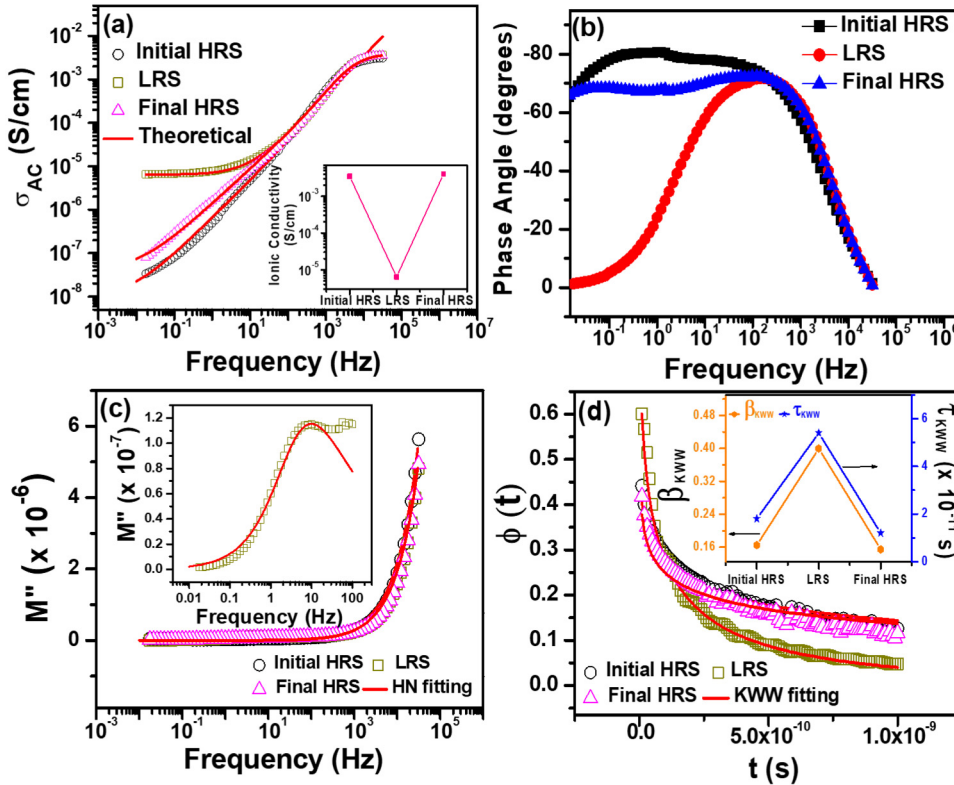


FIG. 8. (a) AC conductivity spectra of the memristive device at initial HRS, LRS, and final HRS at 300 K. Solid lines are the fits of the experimental data to Eqs. (1) and (2), respectively, (b) bode plot of the as-fabricated device at initial HRS, LRS, and final HRS in the frequency range of 40 kHz to 10 mHz, (c) frequency dependence of imaginary part (M'') of electric modulus at the different states of the as-fabricated memristive device and the solid lines are fits of the experimental data to Eq. (3), (d) relaxation function, $\phi(t)$ shown as a function of time at initial HRS, LRS, and final HRS of the device. The solid lines are fits of the calculated HN relaxation function with the stretched exponential KWW decay function [Eq. (6)]. The inset shows the variation of the stretched exponent (β_{KWW}) and the KWW relaxation time (τ_{KWW}) of the charge carriers at the different memristor states.

one site to another neighboring vacant site in the SPE matrix when the frequency is lower than the ion-hopping frequency (ω_p), thus contributing to the ionic conductivity (σ_{ion}) in the as-fabricated device, which comes out as $\sim 6.4 \times 10^{-6}$ S/cm at 300 K during LRS. The transition from the frequency-independent region to the high-frequency dispersive region indicates the onset of the conductivity relaxation process. The relaxation at frequencies above ω_p arises from the polymer segmental motion in the SPE of the memristive device. However, it is to be mentioned here that Eq. (1) is unable to reproduce the experimental AC conductivity results of the memristive device during both the initial and final HRS at lower frequencies, since the AW formalism is not applicable in the low-frequency regime where the electrode polarization is dominant.

The frequency-dependent complex AC conductivity of the device at HRS was analyzed by considering the fractal nature of the electrode-SPE interface, which is given as³²

$$\sigma(\omega) = \sigma_0 + \frac{\sigma_{ion} - \sigma_0}{1 + (i\omega\tau_j)^{-\alpha}} + i\omega\epsilon_0[\epsilon_{relax}(\omega) - \epsilon_\infty], \quad (2)$$

where σ_{ion} is the ionic conductivity of the Li^+ ions in the device, σ_0 is the conductivity at constant electric field, ϵ_0 is the vacuum permittivity (8.854×10^{-14} F/cm), $\epsilon_{relax}(\omega)$ determines the contribution of the dielectric relaxation part, ϵ_∞ is the high-frequency limiting value of dielectric permittivity, τ_j is the characteristic relaxation time, and α is a constant determining the fractal dimension

of the space-time ensemble in the space-charge region having its value lies between 0 and 1. The real part of the frequency-dependent conductivity spectra of the device in both the initial and final HRS are fitted using Eq. (2) and are shown in Fig. 8(a). The values of α are found to be less than unity (~ 0.8), which indicates the fractal dimension of the electrode-electrolyte interface. The charge-carrier relaxation time (τ_j) corresponding to both the initial and final HRS of the as-fabricated device comes out as $\sim 10^{-5}$ s. Both the HRS of the device exhibit a high ionic conductivity (σ_{ion}) of $\sim 4 \times 10^{-3}$ S/cm at 300 K, which is three orders of magnitude higher compared to the LRS of the device. The Nyquist plots at different states of the as-fabricated memristive device are shown in Fig. S9(a) (supplementary material). It is noteworthy to mention that the values of the ionic conductivity (σ_{ion}) in the device obtained from the Nyquist plots are almost the same as those obtained from Eqs. (1) and (2), respectively.

Thus, the distinct plateaus observed in the conductivity spectra at different frequency regimes reflect the presence of two dominant conduction components: bulk ionic conduction and interfacial polarization effects. In the high-resistance states (both initial and final HRS), the low-frequency dispersive region originates from space-charge accumulation at the electrode | SPE interface, whereas the high-frequency plateau is attributed to the hopping motion of Li^+ ions within the polymer matrix, as captured by the fractal model [Eq. (2)]. This suggests that the total resistivity in HRS is primarily governed by ion migration and relaxation

dynamics in the bulk and at the interface. In contrast, during LRS, the frequency-independent conductivity plateau in the low-frequency region and the transition to dispersive behavior at higher frequencies, well-fitted by the Almond–West formalism [Eq. (1)], indicate a different dominant mechanism—filamentary conduction through electrochemically formed lithium bridges. This transition from HRS to LRS is not purely field-driven; rather, it is mediated by coupled ionic and electronic processes, where Li^+ ions migrate under the applied bias and undergo reduction at the counter electrode, leading to metallic filament growth. These filaments establish a percolative electronic path, drastically lowering the device resistance. Upon field removal or reverse bias, the filaments dissolve or rupture, returning the device to the HRS, where ionic conduction dominates once again. Thus, the resistive switching behavior is governed by a reversible transition between ionic conduction in the bulk and interface (HRS) and metallic filament-assisted electronic conduction (LRS).

The Bode plots of the device at different states of the memristive device are shown in Fig. 8(b). It is observed that the phase angle at LRS tends to be zero at the lower frequencies, while the value is quite high at the lower frequency regime during HRS and the largest phase angle of $\sim -63^\circ$ is observed at 10 mHz, inferring good capacitive behavior of the device at both the initial and final HRS of the device. This near-zero phase angle at low frequencies in the LRS reflects the formation of a conductive lithium filament bridging the electrodes, resulting in dominant electronic conduction with predominantly resistive characteristics. Conversely, at the initial and final HRS, the device current is primarily governed by ionic conduction through Li^+ ion hopping within the polymer matrix, coupled with polymer chain segmental motion. The pronounced phase angle in these states is indicative of significant capacitive effects arising from charge accumulation at the electrode–electrolyte interface, which is typical of electrode polarization. Thus, the phase angle behavior clearly distinguishes the transition from a capacitive ionic conduction regime in HRS to a resistive electronic conduction regime in LRS during resistive switching.

To get further insights into the ionic relaxation phenomenon in the device during different memristive states, electric modulus spectra have been studied, which suppress the electrode polarization effects in the low-frequency regime. The frequency dependence of the imaginary part of the electric modulus (M'') at initial HRS (OFF state), intermediate LRS (ON state), and final HRS (RESET state) of the as-fabricated device is shown in Fig. 8(c) at 300 K. It is observed that M'' shows a long tail-like feature at the low-frequency region with an increasing trend at the higher frequency regime during both HRS, indicating the capacitive nature of the device, while at LRS, M'' shows a distinct relaxation shoulder peak at low frequency [as shown in the inset of Fig. 8(c)] followed by a high-frequency dispersive region. The frequency of the peak of M'' spectra is attributed to the conductivity relaxation frequency (ω_c). The conductivity relaxation time (τ_c) can be obtained from the relation, $\omega_c \tau_c = 1$. Below ω_c , mobile Li^+ ions exhibit long-range hopping motion, while above ω_c , Li^+ ions exhibit short-range localized motion in the SPE matrix of the memristive device.

The complex electric modulus spectra are analyzed using the Havriliak–Negami (HN) function given by^{53,54}

$$M^* = M_\infty + \frac{M_s - M_\infty}{[1 + (j\omega\tau_c)^{\alpha_{\text{HN}}}]^{\gamma_{\text{HN}}}}, \quad (3)$$

where M_∞ and M_s are the high-frequency and low-frequency limiting values of the electric modulus spectra, respectively, τ_c is the conductivity relaxation time, and α_{HN} and γ_{HN} are the shape parameters with $0 < \alpha_{\text{HN}} \leq 1$ and $0 < \gamma_{\text{HN}} \leq 1$. For Debye relaxation, the value of both the shape parameters should be unity. The HN fits of the experimental M'' spectra at initial HRS, LRS, and final HRS of the device are shown in Fig. 8(c). The shape parameters as obtained from the best fits at different memristive states are shown in Fig. S9(b) (supplementary material). It is observed that the values of both α_{HN} and γ_{HN} are found to be less than unity at all the states, indicating that the nature of the ion relaxation phenomenon is of non-Debye type in the device. This is also evident from the multi-frequency relaxation peak characteristics at the LRS of the device, i.e., a shoulder peak at low frequency ($\tau_c \sim 43$ ms) followed by an increasing trend at the higher frequency regime, which indicates that the relaxation peak might be observed at higher frequencies. The Havriliak–Negami (HN) function is adopted in this electric modulus formalism due to its capability to accurately describe this non-Debye relaxation behavior arising from heterogeneous ionic environments and structural disorder within the SPE matrix of the as-fabricated device.

For a quantitative analysis of the modulus data in the time domain, the relaxation function, $\varphi(t)$, giving the time evolution of the electric field within the SPE of the memristive device is studied. The complex electric modulus, $M^*(\omega)$, is expressed in terms of the Fourier transform of the decay function $\varphi(t)$ given by⁵⁴

$$M^*(\omega) = M_\infty \left[1 - \int_0^\infty e^{-j\omega t} \left(-\frac{\partial \varphi(t)}{\partial t} \right) dt \right]. \quad (4)$$

The relaxation function in the time domain can be calculated using the inverse transform of Eq. (4) and is given by⁵⁵

$$\varphi(t) = \frac{2}{\pi} \int_0^\infty \frac{M''}{\omega M_\infty} \cos(\omega t) d\omega. \quad (5)$$

The inverse transform is performed for different memristive states using the modulus HN equation [Eq. (4)] keeping the parameters same as obtained from the fitting of the experimental M'' spectra. The time dependence of $\varphi(t)$ obtained from Eq. (5) at initial HRS, LRS, and final HRS of the device is shown in Fig. 8(d). For non-Debye type relaxations, the relaxation function is approximated by the KWW or stretched exponential decay function given by⁵⁶

$$\varphi(t) \approx \exp \left[-\left(\frac{t}{\tau_{\text{KWW}}} \right)^{\beta_{\text{KWW}}} \right], \quad (6)$$

where β_{KWW} is the stretched exponent lying between 0 and 1 and τ_{KWW} is the relaxation time. The $\varphi(t)$ curves at different memristive states are fitted to Eq. (6) and are shown in Fig. 8(d). The variation of β_{KWW} and τ_{KWW} at initial HRS, LRS, and final HRS of the device,

as obtained from the best fits, is shown in the inset of Fig. 8(d). The small values of β_{KWW} (<1) are an indication of highly non-exponential relaxation behavior in all the states, suggesting non-Debye type relaxation of the Li^+ ions in the device. It is to note here that the relaxation time, τ_{KWW} , is the lowest at both HRS, as expected from the high ionic conductivity results at HRS. This indicates the increase in the long-range hopping motion of the Li^+ ions along the polymer chains in the SPE matrix of the device at HRS. This also suggests that the Li^+ motion is coupled with the polymer segmental motion, resulting in the shifting of the M'' peak toward the higher frequency range. The relation between HN shape parameters (α_{HN} and γ_{HN}) and KWW stretched exponent (β_{KWW}) has been given by $\beta_{\text{KWW}} = (\alpha_{\text{HN}}\gamma_{\text{HN}})^{1/23}$, which is being obeyed by the fitting parameters at all the states of the as-fabricated device.⁴⁷ This indicates that both the HN and KWW representations are valid with the same physical significance for different memristive states of the device.

This comprehensive analysis of the AC conductivity, electric modulus, and relaxation dynamics across different resistive states offers deep mechanistic insight into the memristive behavior of the device. By successfully applying both Almond–West and fractal models, this study demonstrates the distinct ionic transport mechanisms in low- and high-resistance states, revealing the critical roles of Li^+ ion hopping, electrode polarization, and polymer segmental motion. The identification of non-Debye type relaxation through Havriliak–Negami and KWW formalisms underscores the complexity of ion dynamics in the SPE matrix and their coupling with the polymer backbone. These findings not only provide key quantitative parameters such as ion-hopping frequency, conductivity relaxation time, and fractal interfacial characteristics but also establish a unified framework to interpret switching phenomena from both frequency and time domain perspectives. Importantly, this work lays the groundwork for rational design of solid-state memristive devices by correlating microscopic ion transport processes with macroscopic switching behavior, thereby advancing the development of high-performance, reliable, and energy-efficient memory technologies.

To explore the reliability of the dual-functional properties of the as-fabricated device, I–V sweep measurements were again performed on the device in the sweep range of -3 to $+3$ V (i.e., 6 V voltage window) from a higher current compliance value (I_{cc}) of $200\ \mu\text{A}$ (memristive state) to lower I_{cc} values, in order to switch the device back to the supercapacitive (SC) state. It is evident from Fig. S10(a) (supplementary material) that the device under study can be successfully switched from the memristive to the SC state at lower I_{cc} values ranging from 0.5 to $50\ \mu\text{A}$. A clear transition from a typical pinched hysteresis loop (with zero crossing) at higher $I_{\text{cc}} = 200\ \mu\text{A}$ to a leaf-shaped capacitive loop at lower I_{cc} values is observed [as shown in Fig. S10(a) in the supplementary material]. The I–V sweep measurements at a lower I_{cc} value of $50\ \mu\text{A}$ with a voltage scan rate of $500\ \text{mV/s}$ are compared for both the initial SC state (before voltage pulsing) and the final SC state (after voltage pulsing), as shown in Fig. S10(b) (supplementary material). The areal capacitance of the device does not differ much in both states ($\sim 0.02\ \text{mF/cm}^2$), inferring good stability performance of the as-fabricated device. Further to examine the kinetics of the Li^+ ions in the device, electrochemical impedance spectroscopy (EIS) has been performed after switching the device back to the SC state from the initial memristive HRS state. The Nyquist plots are compared for

both the switching states, i.e., the initial memristive HRS and the final SC state over the frequency range of $40\ \text{kHz}$ to $10\ \text{mHz}$, as shown in Fig. S10(c) (supplementary material). It is clear that both the values of R_s and R_{ct} are very low for both the states. Low R_s indicates intimate contact between the electrode and SPE, while low R_{ct} suggests better ion diffusion at the electrode/SPE interface. The frequency dependence of the real part of the capacitance (C_{re}) at both the switching states is shown in Fig. S10(d) (supplementary material). It is observed that the value of C_{re} at the final SC has been increased ($\sim 0.083\ \text{mF}$ at $10\ \text{mHz}$), as compared to the initial memristive HRS ($\sim 0.047\ \text{mF}$ at $10\ \text{mHz}$), which infers excellent switching and capacitive stability of the as-fabricated device.

III. CONCLUSION

The present work demonstrates the development of a novel, dual-functional solid-state symmetric coin-type device that exhibits both supercapacitive and memristive characteristics, using a nano-structured ZnO electrode and a blended chitosan (CS)/polyvinylidene fluoride (PVDF) solid polymer electrolyte (SPE) film. The device showed a stable electrochemical performance, with a maximum areal capacitance of $1.66\ \text{mF/cm}^2$ and an electrochemical stability window (ESW) of $4\ \text{V}$, making it a promising candidate for energy storage applications. Moreover, the memristive behavior, activated under higher current compliance, demonstrated short-term potentiation (STP) and long-term potentiation (LTP), mimicking the neural synaptic behavior. Additionally, the lithium filament growth dynamics in the SPE facilitated a controlled switching behavior between high resistance (HRS) and low resistance states (LRS), affirming the potential for integrating this device in neuromorphic computing systems.

In addition to demonstrating dual-mode functionality, the device exhibited consistent, reproducible, and excellent switching between the memristive and supercapacitive states across multiple operational cycles. The transitions were characterized by stable retention behavior and minimal degradation in performance over repeated switching events, underscoring the robustness of the underlying ionic–electronic transport mechanisms. While systematic endurance testing over multiple cycles was beyond the immediate scope of this work, the observed reversibility and stability in both functional regimes provide a strong indication of the potential of the device for long-term operation. Specifically, since both ZnO and chitosan are moisture-sensitive materials, future studies will focus on assessing the effects of humidity and air exposure on device durability and performance. These forthcoming investigations will enable optimization of the device for practical real-world applications, including neuromorphic computing and energy storage technologies. The present findings establish a solid groundwork for comprehensive endurance testing and environmental stability assessments critical for device commercialization.

IV. EXPERIMENTAL SECTION

A. Synthesis of the blended CS/PVDF solid polymer electrolyte (SPE)

The solid polymer electrolytes (SPEs) were synthesized through a solution blending and solvent casting technique. Initially,

16 August 2025 05:16:43

20 wt. % chitosan (CS) (medium molecular weight, $\geq 75\%$ deacetylated, Sigma-Aldrich) and 80 wt. % polyvinylidene fluoride (PVDF, $\geq 99\%$, Alfa Aesar) were separately dissolved in solvents; CS in 50 ml of 1% aqueous acetic acid ($\geq 99.7\%$, Merck) and PVDF in 30 ml of dimethylformamide (DMF, anhydrous, 99.8%, Sigma-Aldrich). The two solutions were then mixed and stirred at room temperature for 10 min to achieve a uniform mixture. Subsequently, lithium perchlorate (LiClO_4 , 99.99%, Sigma-Aldrich) at 80 wt. % as the ionic salt and glycerol ($\geq 99\%$, Sigma-Aldrich) at 15 wt. % as a plasticizer were added to the CS/PVDF blend. The mixture was stirred continuously until a homogeneous viscous solution was obtained. The resulting solutions were cast onto polypropylene petri dishes and dried in a hot air oven at 40°C for 24 h to form solid polymer films (thickness $\sim 280\ \mu\text{m}$). The surface morphology of the SPE was characterized by field emission scanning electron microscopy (FE-SEM) (model: Apreo 2 S, Thermofisher). Thermal properties were evaluated using differential scanning calorimetry (DSC) with a DSC 250 TA Instrument. Measurement was performed in the temperature range of -90 – 75°C at a constant heating rate of $10^\circ\text{C}/\text{min}$. Fourier transform infrared (FTIR) spectroscopy was conducted using a Perkin Elmer FT-IR Spectrum 2 spectrometer with a resolution of $4\ \text{cm}^{-1}$.

B. Device fabrication

For the fabrication of the coin-type symmetric device, a glass substrate was first cleaned sequentially using acetone ($\geq 99.5\%$, Sigma-Aldrich), isopropyl alcohol (IPA, $\geq 99.9\%$, Merck), and distilled water. Current collectors were then prepared by depositing a $\sim 5\ \text{nm}$ layer of titanium (Ti) followed by a $\sim 30\ \text{nm}$ layer of gold (Au) on the cleaned glass substrates through e-beam evaporation ($\sim 10^{-6}$ Torr) at a deposition rate around $0.5\ \text{\AA}/\text{s}$. The cathode and the anode were prepared from a zinc acetate precursor solution, consisting of 109 mg of zinc acetate dihydrate $[\text{Zn}(\text{CH}_3\text{COO})_2 \cdot 2\text{H}_2\text{O}]$, $\geq 99\%$, Sigma-Aldrich, $30.5\ \mu\text{l}$ of ethanolamine ($\geq 99\%$, Merck), and 1 ml of methoxyethanol ($\geq 99\%$, Merck), which was stirred for $\sim 2\ \text{h}$ and filtered through a $0.45\ \mu\text{m}$ PTFE syringe filter. A $100\ \mu\text{l}$ of the filtered zinc acetate solution was spin-coated onto the current collector at 4000 rpm for 50 s. The coated substrate was then annealed at 400°C for 5 min to convert the zinc acetate into a zinc oxide (ZnO) layer (thickness $\sim 45\ \text{nm}$). Finally, the synthesized CS/PVDF solid polymer electrolyte (SPE) was placed between the ZnO-based cathode and anode, forming the complete coin-cell structure. The device was carefully sealed to ensure intimate and uniform interfacial contact between the SPE and the electrode surfaces, effectively eliminating any interfacial voids or air gaps. This precise sealing not only maintains physical confinement of the active layers but also prevents ambient air ingress, thereby preserving the integrity of the electrical and impedance measurements throughout device operation. The ZnO layer was characterized by x-ray diffraction (x-ray diffractometer model: Bruker D8) using the $\text{CuK}\alpha$ radiation of wavelength $1.5406\ \text{\AA}$. Electrochemical measurements were conducted in a two-electrode configuration using a CH Instruments 660E (Austin, TX, USA) after making silver paste contact with the metallic Au electrodes.

C. Calculations

The areal capacitance (C_{areal}) of the device, calculated using Eqs. (7) and (8) from CV and GCD, respectively, is given as follows:

$$C_{\text{areal}} = \frac{\text{Integral area of CV loop}}{\text{Scan rate} \times \Delta V \times A}, \quad (7)$$

$$C_{\text{areal}} = \frac{2I}{\frac{\Delta V}{\Delta t} \times A}, \quad (8)$$

where ΔV is the potential window (V), A is the active area (cm^2), I is the charging current (A), and Δt is the discharging time (s).

Capacitance is a complex quantity, $C(\omega) = C_{\text{re}}(\omega) - jC_{\text{im}}(\omega)$, whose real part $C_{\text{re}}(\omega)$ (generally represented as C_p which is defined as the usable capacitance of the device) and the imaginary part $C_{\text{im}}(\omega)$ are calculated using the following equations:

$$C_{\text{re}}(\omega) = -\frac{Z_{\text{im}}(\omega)}{\omega |Z(\omega)|^2}, \quad (9)$$

$$C_{\text{im}}(\omega) = \frac{Z_{\text{re}}(\omega)}{\omega |Z(\omega)|^2}, \quad (10)$$

where $Z_{\text{re}}(\omega)$ and $Z_{\text{im}}(\omega)$ are the real and imaginary parts of impedance, respectively, and ω is the frequency.

SUPPLEMENTARY MATERIAL

See the [supplementary material](#) for additional experimental data of the coin-type symmetric dual-functional device under study.

ACKNOWLEDGMENTS

S.M. expresses thanks to the Department of Science and Technology (DST), India for providing the national postdoctoral fellowship to carry out this work. S.M. also thanks Professor G. U. Kulkarni for his encouragement and valuable suggestions, and the Jawaharlal Nehru Centre for Advanced Scientific Research (JNCASR) for the instrumental facilities.

AUTHOR DECLARATIONS

Conflict of Interest

The authors have no conflicts to disclose.

Author Contributions

Simantini Majumdar: Conceptualization (equal); Data curation (equal); Formal analysis (equal); Funding acquisition (equal); Investigation (equal); Methodology (equal); Project administration (equal); Resources (equal); Software (equal); Supervision (equal); Validation (equal); Visualization (equal); Writing – original draft (equal); Writing – review & editing (equal).

DATA AVAILABILITY

The data that support the findings of this study are available within the article and its [supplementary material](#).

REFERENCES

- ¹S. G. Kim, J. S. Han, H. Kim, S. Y. Kim, and H. W. Jang, *Adv. Mater. Technol.* **3**, 1800457 (2018).
- ²M. Prezioso, F. Merrikh-Bayat, B. D. Hoskins, G. C. Adam, K. K. Likharev, and D. B. Strukov, *Nature* **521**, 61–64 (2015).
- ³W. Wan, R. Kubendran, C. Schaefer, S. B. Eryilmaz, W. Zhang, D. Wu, S. Deiss, P. Raina, H. Qian, B. Gao, S. Joshi, H. Wu, H. S. P. Wong, and G. Cauwenberghs, *Nature* **608**, 504–512 (2022).
- ⁴M. Rao, H. Tang, J. Wu, W. Song, M. Zhang, W. Yin, Y. Zhuo, F. Kiani, B. Chen, X. Jiang, H. Liu, H.-Y. Chen, R. Midya, F. Ye, H. Jiang, Z. Wang, M. Wu, M. Hu, H. Wang, Q. Xia, N. Ge, J. Li, and J. J. Yang, *Nature* **615**, 823–829 (2023).
- ⁵B. Bannur and G. U. Kulkarni, *Mater. Horiz.* **7**, 2970 (2020).
- ⁶M. Ismail, U. Chand, C. Mahata, J. Nebhen, and S. Kim, *J. Mater. Sci. Technol.* **96**, 94–102 (2022).
- ⁷J. Park, T.-H. Kim, O. Kwon, M. Ismail, C. Mahata, Y. Kim, S. Kim, and S. Kim, *Nano Energy* **104**, 107886 (2022).
- ⁸T. Tan, Y. Du, A. Cao, Y. Sun, G. Zha, H. Lei, and X. Zheng, *J. Alloys Compd.* **766**, 918–924 (2018).
- ⁹L.-Q. Wang, W.-H. Li, X.-G. Tang, X.-B. Guo, Q.-X. Liu, Y.-P. Jiang, and Z.-H. Tang, *Ceram. Int.* **47**, 5617–5623 (2021).
- ¹⁰A. Betal, J. Bera, A. Sharma, A. K. Rath, and S. Sahu, *ACS Appl. Electron. Mater.* **4**, 1109–1116 (2022).
- ¹¹J.-H. Ryu, B. Kim, F. Hussain, C. Mahata, M. Ismail, Y. Kim, and S. Kim, *Appl. Surf. Sci.* **544**, 148796 (2021).
- ¹²Y. Gao, L. Mi, W. Wei, S. Cui, Z. Zheng, H. Hou, and W. Chen, *ACS Appl. Mater. Interfaces* **7**, 4311–4319 (2015).
- ¹³S. K. Ujjain, G. Singh, and R. K. Sharma, *Electrochim. Acta* **169**, 276–282 (2015).
- ¹⁴D. Kong, Y. Wang, S. Huang, J. Hu, Y. Von Lim, B. Liu, S. Fan, Y. Shi, and H. Y. Yang, *Energy Storage Mater.* **23**, 653–663 (2019).
- ¹⁵S. Majumdar, R. Ray, and P. Sen, *Electrochim. Acta* **385**, 138295 (2021).
- ¹⁶T. Pettong, P. Iamprasertkun, A. Krittayavathananon, P. Sukha, P. Sirisinudomkit, A. Seubsai, M. Chareonpanich, P. Kongkachuichay, J. Limtrakul, and M. Sawangphruk, *ACS Appl. Mater. Interfaces* **8**(49), 34045–34053 (2016).
- ¹⁷S. Majumdar, P. Sen, and R. Ray, *Mater. Res. Bull.* **151**, 111814 (2022).
- ¹⁸I. Shakir, M. Shahid, S. Cherevko, C.-H. Chung, and D. J. Kang, *Electrochim. Acta* **58**, 76–80 (2011).
- ¹⁹J. Yu, X. Gao, Z. Cui, Y. Jiao, Q. Zhang, H. Dong, L. Yu, and L. Dong, *Energy Technol.* **7**(6), 1900018 (2019).
- ²⁰S. Wu, J. Liu, H. Wang, and H. Yan, *Int. J. Energy Res.* **43**(2), 697–716 (2019).
- ²¹F. Barzegar, D. Y. Momodu, O. O. Fashedemi, A. Bello, J. K. Dangbegnon, and N. Manyala, *RSC Adv.* **5**, 107482–107487 (2015).
- ²²F.-H. Kuok, H.-H. Chien, C.-C. Lee, Y.-C. Hao, I.-S. Yu, C.-C. Hsu, I.-C. Cheng, and J.-Z. Chen, *RSC Adv.* **8**, 2851–2857 (2018).
- ²³W. Gao, N. Singh, L. Song, Z. Liu, A. L. M. Reddy, L. Ci, R. Vajtai, Q. Zhang, B. Wei, and P. M. Ajayan, *Nat. Nanotechnol.* **6**, 496–500 (2011).
- ²⁴I. Shaheen, K. S. Ahmad, C. Zequine, R. K. Gupta, A. G. Thomas, and M. A. Malik, *New J. Chem.* **44**(42), 18281–18292 (2020).
- ²⁵I. Shaheen, K. S. Ahmad, C. Zequine, R. K. Gupta, A. G. Thomas, and M. A. Malik, *RSC Adv.* **11**, 23374 (2021).
- ²⁶I. Shaheen, K. S. Ahmad, C. Zequine, R. K. Gupta, A. G. Thomas, and M. A. Malik, *Environ. Technol.* **43**(4), 605–616 (2022).
- ²⁷R. D. Kumar, S. Nagarani, S. Balachandran, C. Brundha, S. H. Kumar, R. Manigandan, M. Kumar, V. Sethuraman, and S. H. Kim, *Surf. Interfaces* **33**, 102203 (2022).
- ²⁸C. T. Altaf, O. Coskun, A. Kumtepe, A. M. Rostas, I. Iatsunskyi, E. Coy, E. Erdem, M. Sankir, and N. D. Sankir, *Sci. Rep.* **12**, 11487 (2022).
- ²⁹M. Yadav, M. Kumar, and N. Srivastava, *Electrochim. Acta* **283**, 1551–1559 (2018).
- ³⁰S. Majumdar, P. Sen, and R. Ray, *Ionics* **28**, 1403–1418 (2022).
- ³¹S. J. Kwon, T. Kim, B. M. Jung, S. B. Lee, and U. H. Choi, *ACS Appl. Mater. Interfaces* **10**, 35108–35117 (2018).
- ³²Y. Xu, S. Pei, Y. Yan, L. Wang, G. Xu, S. Yarlagadda, and T.-W. Chou, *ACS Appl. Mater. Interfaces* **13**, 11774–11782 (2021).
- ³³W. Liu, Z. Li, F. Pan, Q. He, and Q. Zhang, *RSC Adv.* **13**, 34652–34659 (2023).
- ³⁴P. Li, J. Feder-Kubis, J. Kunigkeit, M. Zielińska-Blajet, E. Brunner, J. Grothe, and S. Kaskel, *Angew. Chem. Int. Ed.* **63**, e202412674 (2024).
- ³⁵M. K. Akbari, N. S. Lopa, and S. Zhuikov, *Appl. Surf. Sci.* **669**, 160592 (2024).
- ³⁶A. Wang, C. Chen, L. Liao, J. Qian, F.-G. Yuan, and N. Zhang, *J. Inorg. Organomet. Polym. Mater.* **30**, 1497–1502 (2020).
- ³⁷L. H. Sim, S. N. Gan, C. H. Chan, and R. Yahya, *Spectrochim. Acta Part A: Mol. Biomol. Spectrosc.* **76**, 287–292 (2010).
- ³⁸A. K. Arof, S. Amirudin, S. Z. Yusof, and I. M. Noor, *Phys. Chem. Chem. Phys.* **16**, 1856–1867 (2014).
- ³⁹P. Martins, A. C. Lopes, and S. Lanceros-Mendez, *Prog. Polym. Sci.* **39**, 683–706 (2014).
- ⁴⁰A. Salimi and A. A. Yousefi, *Polym. Test.* **22**, 699–704 (2003).
- ⁴¹T. Boccaccio, A. Bottino, G. Capannelli, and P. Piaggio, *J. Membr. Sci.* **210**, 315–329 (2002).
- ⁴²J. Gomes, J. Nunes Serrado, V. Sencadas, and S. Lanceros-Mendez, *Smart Mater. Struct.* **19**, 065010 (2010).
- ⁴³Y. Peng, B. Sun, and P. Wu, *Appl. Spectrosc.* **62**, 295–301 (2008).
- ⁴⁴Y. Peng and P. Wu, *Polymer* **45**, 5295–5299 (2004).
- ⁴⁵M. Sharma, G. Madras, and S. Bose, *Phys. Chem. Chem. Phys.* **16**, 14792–14799 (2014).
- ⁴⁶X. Cai, T. Lei, D. Sun, and L. Lin, *RSC Adv.* **7**, 15382–15389 (2017).
- ⁴⁷S. Majumdar and R. Ray, *J. Polym. Res.* **28**, 157 (2021).
- ⁴⁸J. F. Gomes, A. C. Garcia, L. H. S. Gasparotto, N. E. de Souza, E. B. Ferreira, C. Pires, and G. Tremiliosi-Filho, *Electrochim. Acta* **144**, 361–368 (2014).
- ⁴⁹S. Majumdar, A. M. Antony, and G. U. Kulkarni, *J. Mater. Chem. A* **13**, 12349 (2025).
- ⁵⁰B. Sun, M. Xiao, G. Zhou, Z. Ren, Y. N. Zhou, and Y. A. Wu, *Mater. Today Adv.* **6**, 100056 (2020).
- ⁵¹D. P. Almond and A. R. West, *Solid State Ion.* **11**, 57 (1983).
- ⁵²A. A. Khamzin, I. I. Popov, and R. R. Nigmatullin, *Phys. Rev. E* **89**, 032303 (2014).
- ⁵³S. Havriliak and S. Negami, *Polymer* **8**, 161 (1967).
- ⁵⁴F. S. Howell, R. A. Bose, P. B. Macedo, and C. T. Moynihan, *J. Phys. Chem.* **78**, 639 (1974).
- ⁵⁵P. Jeevanandam and S. Vasudevan, *J. Chem. Phys.* **109**, 8102 (1998).
- ⁵⁶G. Williams and D. C. Watts, *Trans. Faraday Soc.* **66**, 80 (1970).